

University of Groningen

## Surface and Curve Skeletonization of Large 3D Models on the GPU

Jalba, Andrei C.; Kustra, Jacek; Telea, Alexandru C.

*Published in:*  
IEEE transactions on pattern analysis and machine intelligence

*DOI:*  
[10.1109/TPAMI.2012.212](https://doi.org/10.1109/TPAMI.2012.212)

**IMPORTANT NOTE:** You are advised to consult the publisher's version (publisher's PDF) if you wish to cite from it. Please check the document version below.

*Document Version*  
Publisher's PDF, also known as Version of record

*Publication date:*  
2013

[Link to publication in University of Groningen/UMCG research database](#)

*Citation for published version (APA):*

Jalba, A. C., Kustra, J., & Telea, A. C. (2013). Surface and Curve Skeletonization of Large 3D Models on the GPU. *IEEE transactions on pattern analysis and machine intelligence*, 35(6), 1495-1508.  
<https://doi.org/10.1109/TPAMI.2012.212>

**Copyright**

Other than for strictly personal use, it is not permitted to download or to forward/distribute the text or part of it without the consent of the author(s) and/or copyright holder(s), unless the work is under an open content license (like Creative Commons).

The publication may also be distributed here under the terms of Article 25fa of the Dutch Copyright Act, indicated by the "Taverne" license. More information can be found on the University of Groningen website: <https://www.rug.nl/library/open-access/self-archiving-pure/taverne-amendment>.

**Take-down policy**

If you believe that this document breaches copyright please contact us providing details, and we will remove access to the work immediately and investigate your claim.

*Downloaded from the University of Groningen/UMCG research database (Pure): <http://www.rug.nl/research/portal>. For technical reasons the number of authors shown on this cover page is limited to 10 maximum.*

# Surface and Curve Skeletonization of Large 3D Models on the GPU

Andrei C. Jalba, Jacek Kustra, and Alexandru C. Telea

**Abstract**—We present a GPU-based framework for extracting surface and curve skeletons of 3D shapes represented as large polygonal meshes. We use an efficient parallel search strategy to compute point-cloud skeletons and their distance and feature transforms (FTs) with user-defined precision. We regularize skeletons by a new GPU-based geodesic tracing technique which is orders of magnitude faster and more accurate than comparable techniques. We reconstruct the input surface from skeleton clouds using a fast and accurate image-based method. We also show how to reconstruct the skeletal manifold structure as a polygon mesh and the curve skeleton as a polyline. Compared to recent skeletonization methods, our approach offers two orders of magnitude speed-up, high-precision, and low-memory footprints. We demonstrate our framework on several complex 3D models.

**Index Terms**—Medial axes, geodesics, skeleton regularization

## 1 INTRODUCTION

**S**KELETONS, or medial axes, are shape descriptors used in virtual navigation, shape matching, shape reconstruction, and shape processing [62]. Three-dimensional shapes admit two types of skeletons. *Surface skeletons* are 2D manifolds which contain the loci of maximally inscribed balls in a shape [50], [62]. *Curve skeletons* are 1D curves which are locally centered in the shape [16]. Surface-skeleton points, together with their distance to the shape and closest shape points, define the medial surface transform (MST) which is used for animation, smoothing, and matching [4], [6], [17].

Computing *surface* skeletons of complex 3D objects represented by polygonal meshes is still a difficult problem. Challenges include:

1. finding accurate skeletons,
2. removing spurious skeleton branches (i.e., regularizing skeletons),
3. producing skeleton-mesh models for use in subsequent algorithms,
4. efficient computation with respect to speed and memory.

In this paper, we present a framework for computing surface and curve skeletons which fulfills the above requirements, with the following contributions:

- A.C. Jalba is with the Department of Mathematics and Computer Science, Eindhoven University of Technology, PO Box 513, 5600 MB Eindhoven, The Netherlands. E-mail: A.C.Jalba@tue.nl.
- J. Kustra is with Philips Research, High Tech Campus HTC36 P 50, Eindhoven, The Netherlands. E-mail: jacek.kustra@gmail.com.
- A.C. Telea is with the Johann Bernoulli Institute for Mathematics and Computer Science, University of Groningen, PO Box 407, 9700 AK Groningen, The Netherlands. E-mail: a.c.telea@rug.nl.

Manuscript received 29 May 2012; revised 31 Aug. 2012; accepted 5 Sept. 2012; published online 1 Oct. 2012.

Recommended for acceptance by H. Bischof.

For information on obtaining reprints of this article, please send e-mail to: tpami@computer.org, and reference IEEECS Log Number TPAMI-2012-05-0410.

Digital Object Identifier no. 10.1109/TPAMI.2012.212.

- A refinement of the skeleton extraction method in [40] which exploits CPU and GPU parallelism for increased performance.
- A general-purpose GPU geodesic tracing method which is two magnitude orders faster, and more accurate, than similar techniques. We use this method to efficiently apply global regularization [55] to large skeletons.
- An extension of the above regularization method with a new detector to compute robust curve skeletons.
- A new image-space method to reconstruct shapes directly from the (regularized) MST in real time.
- Accurate extraction of skeleton manifolds from MST clouds.

Section 2 reviews related work. We next present our skeleton cloud extraction (Section 3), image-based reconstruction from skeleton clouds (Section 4), geodesic tracing for regularization (Section 5), curve skeleton extraction (Section 8), and skeleton-mesh reconstruction from skeleton clouds (Section 6). Section 7 compares our work with a recent surface skeleton extractor. Section 9 discusses our results. Section 10 concludes the paper.

## 2 RELATED WORK

Given a shape  $\Omega \subset \mathbb{R}^3$  with boundary  $\partial\Omega$ , we first define its distance transform  $DT_{\partial\Omega} : \mathbb{R}^3 \rightarrow \mathbb{R}^+$ :

$$DT_{\partial\Omega}(\mathbf{x} \in \Omega) = \min_{\mathbf{y} \in \partial\Omega} \|\mathbf{x} - \mathbf{y}\|. \quad (1)$$

The skeleton, or medial axis, of  $\Omega$  is next defined as

$$S(\Omega) = \{\mathbf{x} \in \Omega \mid \exists \mathbf{f}_1, \mathbf{f}_2 \in \partial\Omega, \mathbf{f}_1 \neq \mathbf{f}_2, \|\mathbf{x} - \mathbf{f}_1\| = \|\mathbf{x} - \mathbf{f}_2\| = DT_{\partial\Omega}(\mathbf{x})\}, \quad (2)$$

where  $\mathbf{f}_1$  and  $\mathbf{f}_2$  are the contact points with  $\partial\Omega$  of the maximally inscribed ball in  $\Omega$  centered at  $\mathbf{x}$  [28], [55]. The contact points  $\mathbf{f}_1$  and  $\mathbf{f}_2$  are also called *feature transform* (FT) points [65]. The vectors  $\mathbf{f} - \mathbf{x}$  determined by skeleton

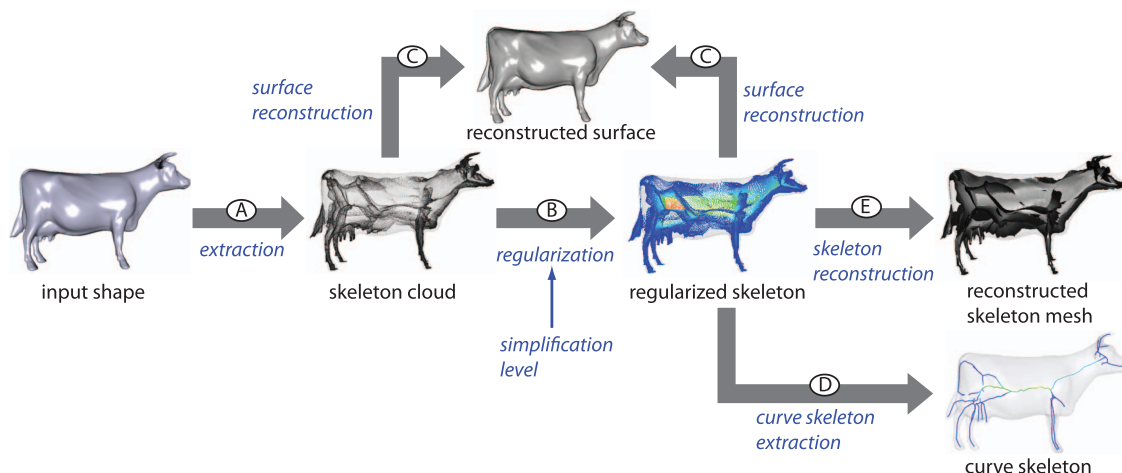


Fig. 1. Our pipeline: Skeleton cloud extraction (A), regularization (B), surface reconstruction (C), curve-skeleton extraction (D), and skeleton-mesh reconstruction (E). All steps except E (CPU-only) are implemented on both the CPU and GPU.

points and their corresponding feature points are also called *spoke vectors* [63].  $S(\Omega)$  is a set of manifolds with boundaries which meet along a set of Y-intersection curves [13], [18], [37].  $S(\Omega)$  can be computed by various methods, as follows.

*Voxel-based methods* include thinning, distance-field, and general-field methods. Thinning removes  $\partial\Omega$  voxels (or pixels in 2D) while preserving connectivity [7], [48]. Voxel removal in distance-to-boundary order enforces centeredness [53]. Distance-field methods find  $S(\Omega)$  along singularities of  $DT_{\partial\Omega}$  [27], [31], [35], [38], [56], [60], [71], [74] and can be efficiently done on GPUs [11], [65], [67], [72]. General-field methods use fields smoother (with fewer singularities) than distance transforms [1], [4], [16], [30]. Such methods are more robust for noisy shapes. Foskey et al. compute the  $\theta$ -SMA, an approximate simplified medial axis, using the angle between feature vectors [24]. The  $\theta$ -SMA can get disconnected along the so-called ligature branches. The  $\theta$ -HMA refines the  $\theta$ -SMA by computing medial axes which are homotopy-equivalent to the input surface [67].

*Mesh-based methods* often use Voronoi diagrams to compute polygonal skeletons [21]. Amenta et al. compute the Power Crust, an approximation of a surface and its medial axis by a subset of Voronoi points [3]. Other methods use edge collapses [39], starting from a mesh segmentation [33], or sphere sweeping [44]. Mesh-based methods compute precise 3D skeletons, can handle nonuniformly sampled surfaces, and use much less memory—typically  $O(n^2)$  as compared to  $O(n^3)$  needed for a  $n^3$  voxel volume. However, such methods are quite complex to implement, can be numerically unstable, and are harder to parallelize [66].

Clean skeletons are extracted from noisy shapes by thresholding *importance measures* to prune points caused by small details [58]. We distinguish between local and global measures [43], [55]. Local measures cannot separate locally identical, yet globally different, contexts (see, e.g., [55], Fig. 1). Thresholding local measures can disconnect skeletons. Reconnection needs extra work [41], [50], [60], [67], and makes pruning less intuitive [58]. Local measures include the angle between the feature points and distance-to-boundary [3], [24], divergence-based [9], [60], and first-order

moments [56]. Stolpner et al. find skeleton voxels where the gradient of the shape's distance transform is multivalued [63], [64]. Precision and speed are increased by a voxel-and-point-cloud approach which subdivides voxels close to the skeleton. Leymarie and Kimia topologically simplify point-cloud skeletons to capture Y-intersection curves and skeleton sheet boundaries in medial scaffolds [37]. Good surveys of skeletonization theory are given in [62] and [64].

Global measures monotonically increase from the skeleton boundary inwards. Thresholding them yields connected skeletons. Miklos et al. approximate shapes by a union of balls (UoB) and use UoB medial properties [29] to simplify skeletons [43]. Dey and Sun present the medial geodesic function (MGF), which is equal to the shortest-geodesic length between feature points [20], [52]. Related work on curve skeletons is given in Section 8. Reniers et al. [55] extend the MGF for surface and curve skeletons using geodesic lengths and surface areas between geodesics, respectively, inspired by the so-called 2D collapse metric [17], [47], [71]. Besides monotonicity, the MGF and its 2D collapse metric counterpart have an intuitive geometric meaning: They assign to a skeleton point the amount of shape boundary that corresponds, or “collapses to,” the respective skeleton point. Hence, skeleton points with small metric values correspond to small-scale shape details, and skeleton points with large metric values correspond to large-scale shape details. This allows an easy simplification of the skeleton: Thresholding by a value  $\tau$  eliminates all skeleton points which encode less than  $\tau$  boundary length units. However, for large 3D meshes, computing the geodesics required to evaluate the MGF is an expensive process.

Recently, Ma et al. proposed arguably the fastest method to extract surface skeletons from oriented point clouds [40]. However, this method produces a “raw” surface-skeleton *point cloud* which, as the authors note too, are of limited use if one requires a compact skeleton surface or a curve skeleton. We extend their proposal in several directions (see Fig. 1): (A) faster skeleton-cloud extraction, (B) regularization, (C) object reconstruction, (D) curve-skeleton extraction, and (E) surface-skeleton mesh reconstruction. These steps are described next.

TABLE 1  
Performance of Our Skeleton Extraction Method on Both CPU and GPU (See Section 3)

Model	Points (surface)	Points (skeleton)	CPU timings ( $t$ seconds, $k$ iterations)						GPU timings	
			$\tau = 10^{-4}, \varepsilon = 0$		$\tau = 10^{-3}, \varepsilon = 0$		$\tau = \varepsilon = 10^{-3}$		$\tau = 10^{-3}, \varepsilon = 0$	
			k	t	k	t	k	t	k	t
Armadillo	106289	106289	5	1.29	3	0.87		0.87		0.21
Dragon	437645	436439	5	6.53	2	5.46		5.44		1.21
Horse	48485	48485	5	0.77	3	0.58		0.58		0.09
Cow	185882	185703	5	3.63	3	2.82		2.77		0.64
Bird	46866	46862	5	0.44	3	0.35		0.34		0.03
Horse 2	193934	193887	5	7.51	3	5.77		5.77		1.32
Asiandragon	231574	230964	4	2.83	2	2.19		2.19		0.22
Asiandragon 2	954027	951010	5	17.12	3	13.10		11.82		1.57
Hand	197245	196920	4	3.32	2	2.50		2.50		0.51
Elephant	50485	50422	5	0.62	3	0.48		0.48		0.05
Buddha	543652	541762	4	6.76	3	5.47		5.37		1.42
Mouse	403652	402301	6	5.61	3	3.07		3.02		0.34
Pig	225282	224539	5	7.48	3	4.21		4.17		1.47
Armadillo 2	172974	172955	6	3.29	3	1.86		1.86		0.47
Rabbit	124998	123811	6	1.31	3	0.85		0.83		0.06

### 3 SURFACE SKELETON EXTRACTION

Given an input shape  $\partial\Omega$ , we extract a skeleton point-cloud from an oriented point-cloud model  $C = \{(\mathbf{p}_i, \mathbf{n}_i)\}$  containing points  $\mathbf{p}_i$  and their surface normals  $\mathbf{n}_i$ , where the point coordinates are normalized to  $[-1, 1]^3$  for simplicity. Our method is based on the ball shrinking algorithm of Ma et al. [40], which works as follows: For each point  $\mathbf{p} \in C$ , a (large) ball  $B(\mathbf{s}, r_0) | \mathbf{s} = -r_0\mathbf{n} + \mathbf{p}$ , tangent at  $\mathbf{p}$ , is created. By definition,  $\mathbf{f}_1 \equiv \mathbf{p}$  is the first feature point of  $\mathbf{s}$ . The algorithm shrinks  $B$  by searching the closest point  $\mathbf{f}_2$  to  $\mathbf{s}$  and iteratively moving  $\mathbf{s}$  so that  $B$  passes through  $\mathbf{f}_1$  and  $\mathbf{f}_2$  until  $\mathbf{s}$  converges. At that moment,  $B$  is maximally inscribed, and its center  $\mathbf{s}$  yields a new skeleton point with inscribed radius  $r_{ins} = \|\mathbf{s} - \mathbf{f}_1\| = \|\mathbf{s} - \mathbf{f}_2\|$ ; for full details see [40]. We next propose two performance improvements for this method.

#### 3.1 CPU Parallelization

Ma et al. propose an efficient sequential CPU implementation. Key to their method is a heuristic that sets the initial radius  $r_0$  for a ball  $B(\mathbf{s}, r_0)$  being shrunk to the radius of a skeleton point already found for a surface point  $\tilde{\mathbf{p}}$  close to  $\mathbf{p}$ . This greatly reduces the number of shrinking steps (see [40], Section 3). However, this requires *sequential* processing of the cloud  $C$  in a global distance-based ordering, computed by in-order visiting a  $kd$  tree containing  $C$ .

We parallelize this idea as follows: We use a single global value  $r_0$ , initially set to 2. Next, we divide  $C$  into  $N$  equal-sized chunks (without any point ordering) and process one chunk per thread. When a thread finds a new value  $r_{ins}$ , we set  $r_0$  to  $(r_0 + r_{ins})/2$ , i.e., adapt  $r_0$  in a moving-average fashion. Additionally, we stop shrinking the ball when two consecutive center positions differ by a value less than a user-specified value  $\tau$ . Finally, we use an *approximate* nearest neighbor (NN) scheme based on  $kd$  trees [45] to search for the closest point  $\mathbf{f}_2$  to  $\mathbf{s}$  with precision  $\varepsilon$ .

Table 1 shows our skeleton extraction timings  $t$  and average number  $k$  of  $kd$ -tree searches per point for different  $\tau$  and  $\varepsilon$  values, on several models, on a 4-core 2.4 GHz CPU with  $N = 8$  threads. For the first three models, timings by the method of Ma et al. are also given in Table 2. Smaller

$\tau$  values need more iterations; larger  $\tau$  values yield less accurate skeletons quicker. We see that  $k$  is quite stable for all models. For a skeleton centeredness precision  $\tau = 10^{-3}$ , our method is roughly four times faster than the sequential method of Ma et al., which also uses a 2.4 GHz CPU. Given our 4-core CPU, this implies a very efficient parallelization. Relaxing  $\varepsilon$  slightly accelerates this search (Table 1, column  $\varepsilon = 10^{-3}$ ) with little accuracy loss.

Ball shrinking yields a surface-skeleton cloud  $S = \{(\mathbf{s}, \mathbf{f}_1, \mathbf{f}_2)_i\}$  with two feature points  $\mathbf{f}_1, \mathbf{f}_2$  per skeleton point  $\mathbf{s}$  (see Fig. 6). The local density of  $S$  is proportional with the input cloud density times the shape curvature [62]. Thus, we get more skeleton points where the surface changes rapidly and/or is finely sampled, see, e.g., the cow's horns, ears, and pig's snout in Fig. 6. Controlling this density is easy: For more points, we refined the initial mesh, using the Yams package [25]. For fewer points, we uniformly subsample  $S$  by removing all points closer to each skeleton point than some distance  $\delta$ . Fig. 2 shows the skeleton of a cow model for four different  $\delta$  values. Conceptually, our method is similar to Leymarie and Kimia [37]: We regard each input point  $\mathbf{f}_1$  as a medial axis "generator" and try to pair it with another point  $\mathbf{f}_2$ , and test maximality of the resulting balls. However, while [37] explicitly computes pairs  $(\mathbf{f}_1, \mathbf{f}_2)$  and checks for ball maximality using search strategies based on visibility constraints, we implicitly compute the pairs *while* shrinking balls.

#### 3.2 GPU Parallelization

For an efficient transfer of ball shrinking to GPUs, we need 1) an efficient GPU nearest neighbor search and 2) an effective load balancing between GPU threads.

TABLE 2  
Performance of the Method by Ma et al. [40]

Model	Points (surface)	CPU timings (seconds)	GPU timings (seconds)
Armadillo	106289	4.20	0.39
Dragon	437645	20.23	2.64
Horse	48485	1.62	0.29

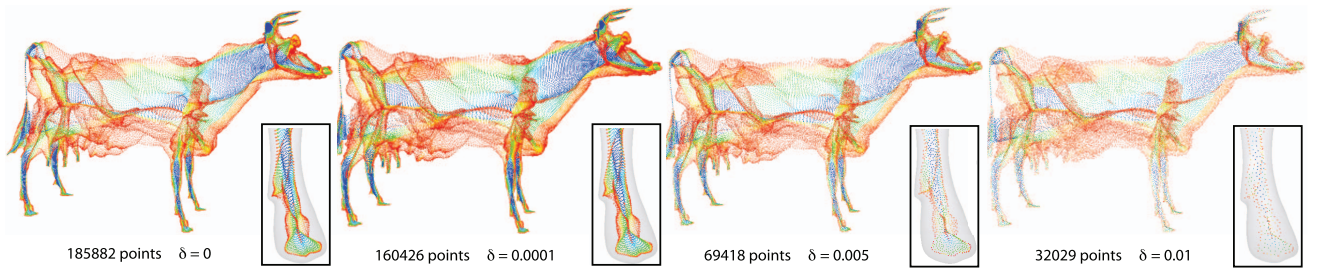


Fig. 2. Uniform skeleton sampling for different  $\delta$  values (see Section 3). Colors show angles of feature vectors ( $\theta$ -SMA detector).

To these ends, Ma et al. proposed a mixed CPU-GPU approach [40]. For NN search, they use the GPU algorithm in [76]. For load balancing, ball-shrinking iterations are done in parallel on the GPU. After *each* GPU iteration, threads ask the CPU whether each ball needs more iterations. If so, the CPU invokes the GPU kernel for the next iteration only for the not-yet-converged balls. As Ma et al. mention, this achieves good performance, but cannot use the initial radius heuristic as that heuristic was designed for a sequential algorithm.

Our GPU proposal directly parallelizes the CPU algorithm with one thread per skeleton point. Since our initial radius heuristic works in a parallel setting, we transfer it directly to the GPU.

In contrast to Ma et al., we use a GPU-only load balancing scheme. This poses some subtle constraints on the choice of the NN technique used. For this, we investigated several options. Garcia et al. showed a GPU brute-force NN algorithm [26] which turned out to be 20 to 30 times slower than our CPU KD-tree search [45]. Cayton's NN algorithm covers the input set of  $N$  points by a randomly distributed set of  $m \ll N$  overlapping balls which are searched in parallel on the GPU [12]. However, this method cannot do several NN searches in parallel, which we need to parallelize ball extraction. Left-balanced GPU KD-trees also perform poorly. Such trees are rather deep (maximum depth  $D = \log N$  for  $N$  input points). Also, the unfavorable distribution of query points (potential skeleton points having at least two shape points at equal distances) causes many tree node visits during an NN search, i.e., many random, uncached, memory accesses which seriously degrade GPU performance.

For our context, a KD-tree with alternating splitting dimensions and median-based pivoting proved best. We limit the tree depth to a small value (10 to 12). Leaf nodes store more than one point and are linearly searched. Linear search performs very well on the GPU [26] (more cache hits and coalesced memory accesses), yielding a better overall NN speed.

Table 1 shows the speed of our GPU method on an Nvidia GTX 280. Since the GPU NN search is exact, these timings should be compared with CPU timings for  $\varepsilon = 0$ . Thus, our GPU method is 4 to 10 times faster than its CPU variant. Compared to the GPU method of Ma et al. (see Table 2), we are about three times faster as we use an initial radius heuristic which their method does not support.

#### 4 IMAGE-BASED SURFACE RECONSTRUCTION

We now present an efficient and simple algorithm for reconstruction of a model from its skeleton cloud (Fig. 3).

For each skeleton point  $s_i$  with radius  $r_i$ , we build a viewplane-aligned quad  $Q$ , or billboard, of world-space edge size 2. We texture  $Q$  scaled to  $(r_i, r_i, 1)$  with a  $D \times D$  texture whose texels  $T(u, v)$  encode both depth and shading. If fixed-point texturing is available,  $T$  uses a 32-bit RGBA format: The first 3 bytes of  $T(u, v)$  encode the height at  $(u/D, v/D)$  of a ball of radius 1 centered in the texture (see insets in Fig. 3). The fourth texture byte (A) encodes the ball color computed, e.g., with Phong shading. If floating-point textures are available, we encode the height and shading in the L and A channels of a luminance-alpha texture. This leaves two texture channels for future potential use. The texture size  $D$  is set to 512. This yields highly accurate shading and height encoding even for very large balls. For maximal rendering speed, we store  $T$  on  $\log_2(D)$  precomputed mip-map levels.

We render the quads by a simple ARB fragment program shader (seven operations), which gets the  $z_{NDC}$  normalized device coordinate (NDC) of the current skeleton point  $s_i$  via the current color. The shader then computes the final NDC depth  $z_{NDC} + h$  at the current pixel from the incoming  $z_{NDC}$  and ball height  $h$  (from the current texel). If  $z + h$  passes the depth test, the current texel's color is copied to the fragment output. The overall effect is as if 3D balls centered at the skeleton points and scaled to the respective skeleton-point radii are rendered with hidden surface removal.

Our method renders shaded models directly from skeleton clouds of 500K points at 15 frames/second on a GT 330M card. If lighting changes, we only recompute one shading texture. The  $x, y$  splat sizes are pixel-accurate (by OpenGL scaling). Depth values are either 24-bit fixed-point

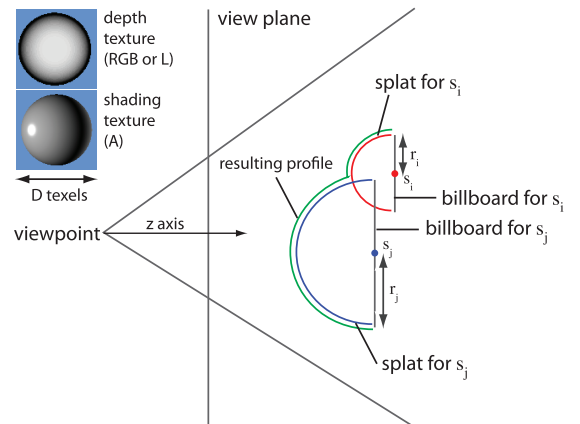


Fig. 3. Skeleton splatting for surface reconstruction.



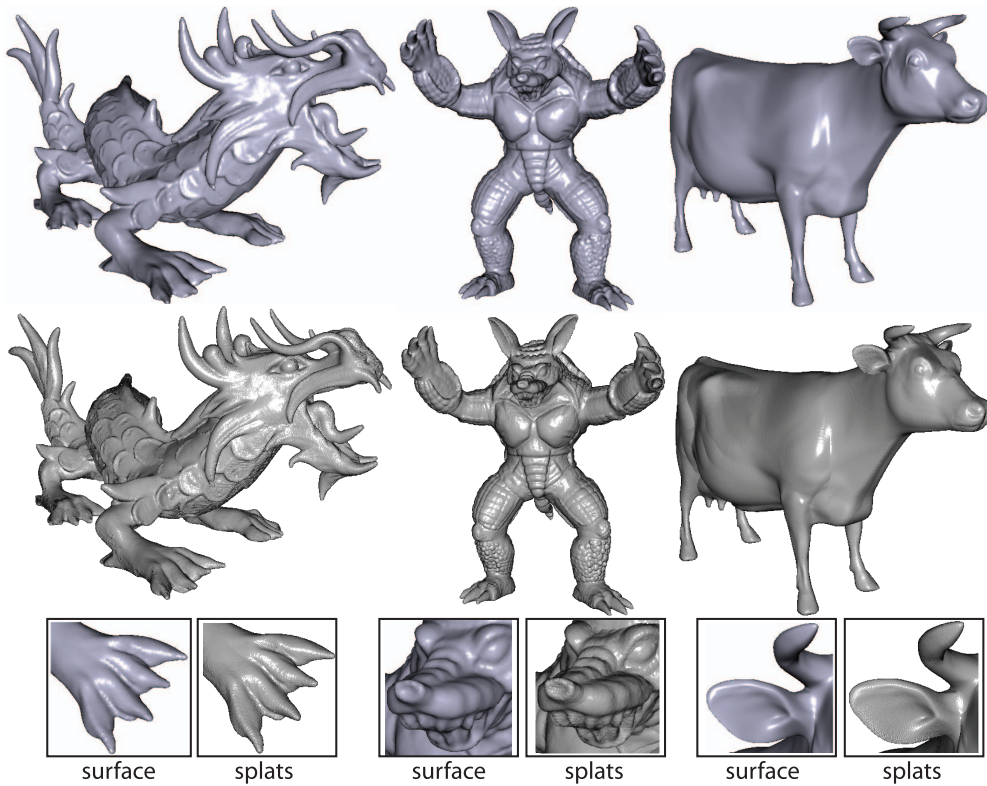


Fig. 4. Comparison of surface rendering (top row) and skeleton image-based surface reconstruction (middle row). Insets show details.

of floating point; hence one can use whichever of the two is readily available on one's platform. Overall, our splatting-based reconstruction method delivers images nearly identical to the original mesh (see Fig. 4).

*Progressive rendering.* like the Qsplat method [57], is easily done by drawing billboards sorted by a skeleton importance metric, e.g., ball radius or our geodesic metric in Section 5. If we use the geodesic metric, this always produces compact shapes. This result cannot be guaranteed by pure surface splatting like Qsplat. Alternatively, using a simplified skeleton as input for the reconstruction allows us to obtain simplified renderings of the input shape. For example, if we use a surface skeleton simplified by the geodesic-based importance metric presented next in Section 5, we obtain a shape where edges have been smoothed out; if we use the curve skeleton presented next in Section 8, we obtain a tubular approximation of the input shape. Other shape simplification effects can be achieved by choosing suitable skeleton simplification metrics.

*Thickness estimation.* Our splatting can also be used to estimate the so-called local shape thickness, also called wall thickness, a known task in 3D metrology [5], [22], [36], [62], [70]. Given a shape  $\Omega \subset \mathbb{R}^3$ , the thickness at a point  $\mathbf{p} \in \partial\Omega$  is defined as the distance from  $\mathbf{p}$  to the closest point on the skeleton  $S(\Omega)$  to  $\mathbf{p}$ . We can efficiently evaluate (and visualize) the thickness at all points on  $\partial\Omega$  by simply mapping the skeleton points' radii  $r_i$  to their splat colors via a gray-to-red (thin-to-thick) colormap (Fig. 5). Reconstructing the shape by ball splatting will now show thin surface areas as red and thick areas as white (see Fig. 5). Compared to typical curvature estimation used for the same task, we need no differentiation and work directly on a point

cloud. Our method is fast: The models in Fig. 5 take under 0.2 seconds with our method and several seconds on identical hardware with a recent voxel-based thickness estimator [70].

*Union of balls.* Our image-based skeleton splatting delivers the same result as a UoB model, e.g., [43], [64]. Our splatting could be used as drop-in shape reconstruction for any method that delivers an MST point cloud. As we shall see in Section 7, our method is roughly one to two orders of magnitude faster than [43] and over two orders of magnitude faster than [64].

## 5 SKELETON REGULARIZATION

*Skeleton regularization* assigns an importance value  $\rho : S \rightarrow \mathbb{R}^+$  to skeleton points (Section 2). If  $\rho$  monotonically increases from the skeleton boundary inwards, thresholding  $\rho$  yields a connected skeleton which captures shape details at a given scale. Such metrics are proposed in [20], [52], and [55]: For a skeleton point  $\mathbf{s}$  with feature points  $\mathbf{f}_1$ ,  $\mathbf{f}_2$ ,  $\rho(\mathbf{s})$  is the length of the shortest path  $\gamma$  on  $\partial\Omega$  between  $\mathbf{f}_1$  and  $\mathbf{f}_2$ . Finding such paths can be done using Dijkstra's

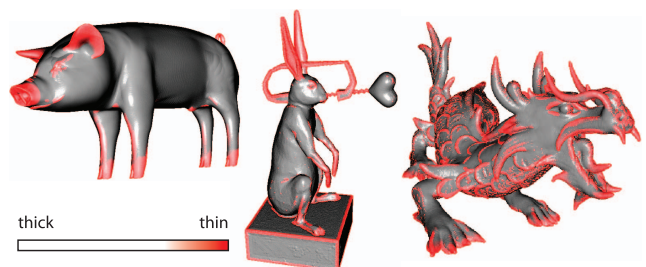


Fig. 5. Thickness estimation using image-based skeleton splatting.

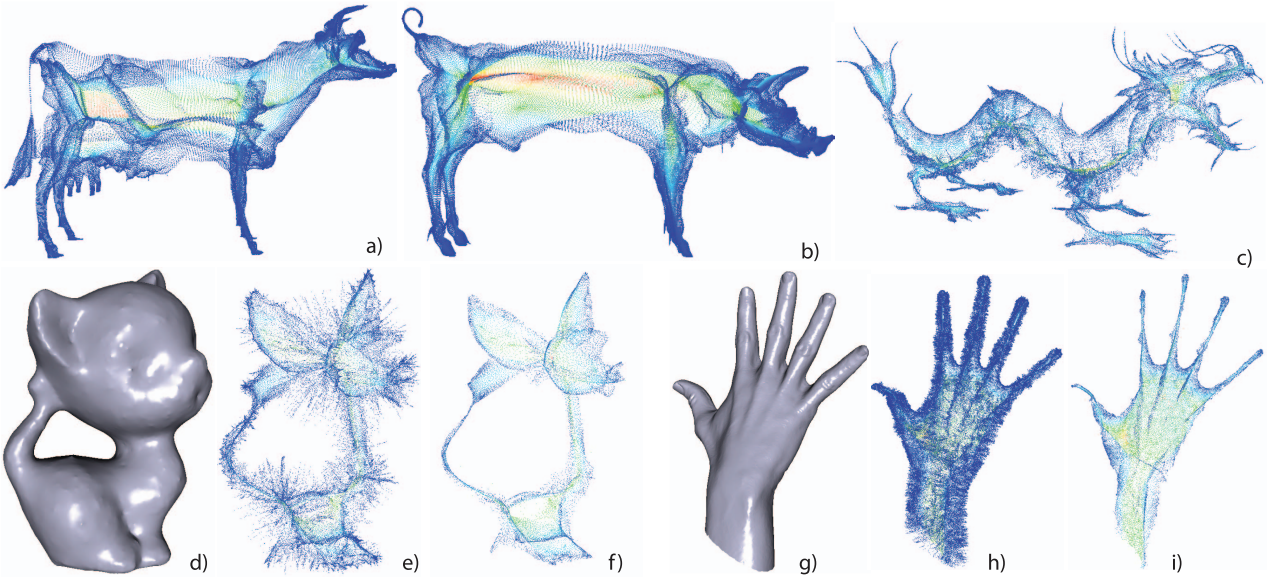


Fig. 6. Skeleton cloud regularization by geodesic importance. Red points are the most important. Blue points correspond to small surface features (Section 5).

algorithm [55], computing the distance map  $DT_{f_1}$  of  $f_1$  by the fast marching method (FMM) and then tracing  $\gamma$  in  $-\nabla DT_{f_1}$  from  $f_2$  [49], or hybrid search techniques [68], [73]. However, such methods are very slow, as we shall see next.

### 5.1 Shortest and Straightest Geodesics

We compute the skeleton importance  $\rho$  using discrete *straightest geodesics* on polyhedral surfaces [32], [51] which generalize straight lines to arbitrary manifolds. Given a point  $\mathbf{p} \in \partial\Omega$  and a tangent vector  $\mathbf{v} \in T_p$  at  $\mathbf{p}$ , the (discrete) straightest geodesic  $\gamma_S$  is the unique solution of the (discrete) initial-value problem  $\gamma_S(0) = \mathbf{p}$ ,  $\gamma'_S(0) = \mathbf{v}$  [51]. We extend this to define the (discrete) *shortest, straightest geodesic* (SSG)  $\gamma_{se}$  between two points  $s, e \in \partial\Omega$ , over tangent vectors  $\mathbf{v}_i \in T_s$  at  $s$ , as the solution of the discrete boundary-value problem:

$$\begin{aligned} \gamma_{S,i}(0) &= \mathbf{s}, \quad \gamma'_{S,i}(0) = \mathbf{v}_i, \\ \gamma_{S,i}(\|\gamma_{S,i}\|) &= \mathbf{e}, \\ \gamma_{se} &= \arg \min_i \|\gamma_{S,i}\|, \end{aligned} \quad (3)$$

where  $\|\gamma_{S,i}\|$  is the length of the discrete geodesic  $\gamma_{S,i}$ . Thus,  $\gamma_{se}$  is the shortest among all straightest geodesics between  $s$  and  $e$ . Solving (3) is not easy. Speed-wise, the cost is proportional to the number of tangent directions  $\mathbf{v}_i$  considered. Also, current algorithms for computing straightest geodesics [32], [51] estimate  $\gamma'$  by evaluating the (discrete) Gaussian curvature at the mesh vertices visited while tracing. The tangent vectors to  $\gamma$  may change directions, especially when this curvature is not exactly  $2\pi$ , so geodesics may not reach their endpoints  $e$ , which is critical for our goal. All these concerns are addressed next.

### 5.2 Efficient SSG Computation

For a skeleton point  $s$ , we trace  $M$  straightest geodesics  $\gamma_{S,i}$ ,  $1 \leq i \leq M$ , in parallel on the CPU or GPU between the feature points  $f_1$  and  $f_2$  of  $s$  on  $\partial\Omega$ , with starting angles  $\alpha_i = (2\pi i)/M$  uniformly spread around the vector

$\mathbf{f} = \mathbf{f}_1 - \mathbf{f}_2$  at  $f_1$ . For each direction  $\mathbf{v}_i$ , we intersect the edges of the mesh faces visited while tracing by the plane with normal  $\mathbf{n}_i = \mathbf{f} \times \mathbf{v}_i$ , and set  $\rho(s) = \min_i \|\gamma_{S,i}\|$ , i.e., the length of the SSG between  $f_1, f_2$ .

We speed up tracing by early termination: We stop tracing a path if its length exceeds the current  $\rho(s)$ . For a closed mesh, we consider both paths from  $f_1$  to  $f_2$  given by the mesh-plane intersection (closed) curve. When one of these paths is computed, we stop tracing the other path if its current length exceeds the first path's length. For a computed  $\gamma_{se}$ , we also store its tangent vectors  $\mathbf{t}_s$  and  $\mathbf{t}_e$  in  $f_1$  and  $f_2$ , respectively, and use  $\mathbf{t}_s$  as starting direction when tracing SSGs for the next skeleton point. Since neighbor skeleton points usually have similar geodesics [20], [54], early termination occurs sooner. This further speeds up tracing.

As shown in Fig. 6,  $\rho$  monotonically increases from the skeleton boundary (blue) inwards (red). Thresholding  $\rho$  removes skeleton points given by small shape details (Figs. 6e, 6f, 6h, and 6i). Such details can be surface noise (Fig. 6d), but also appear in locally tubular shapes (Fig. 6f). In contrast, thresholding nonmonotonic metrics such as  $\theta$ -SMA (Fig. 2) would disconnect skeletons.

### 5.3 Performance and Accuracy of SSG Tracing

Table 3 shows the speed of our SSG method on a GTX 280 card *versus* a 2.8 GHz 4-core PC for  $M = 20$  directions, one thread per SSG, and the speed-up due to the heuristics in Section 5.2.

**Speed.** We compared our GPU SSG to FMM [49], the Dijkstra algorithm with  $A^*$  heuristics [55], the Surazhky-approximate (SA) and Surazhky-exact (SE) geodesic tracing [68], and CPU SSG (Section 5.2). Of these, only SA and Dijkstra were used to regularize skeletons [20], [55]. GPU SSG is 3 to 10 times faster than CPU SSG (higher speed-ups for larger models, Table 3), 10 times faster than Dijkstra, 100 times faster than FMM, 500 times faster than SA, and *thousands* of times faster than SE. This is not surprising: For

TABLE 3  
Timings for Computing the Geodesic Importance

Model	Timing CPU (seconds)	Timing GPU (seconds)	Optimization speed-up (%)
Cow	61.7	18.2	67.4
Bird	10.3	3.2	33.4
Horse	78.9	13.6	57.4
Asiandragon	61.5	13.8	60.0
Asiandragon 2	541.2	115.1	57.8
Hand	62.2	3.1	48.1
Elephant	7.1	3.3	57.1
Buddha	327.6	43.4	62.3
Mouse	210.3	52.1	69.0
Dragon	198.3	30.4	57.2
Pig	96.9	24.0	64.5
Armadillo	63.4	11.2	59.3
Rabbit	76.4	10.8	49.2

an  $n$ -vertex mesh, Dijkstra is  $O(n^2 \log n)$ ; FMM computes one distance field per vertex ( $O(n \log n)$ ) and traces a geodesic in this field ( $O(\sqrt{n})$ , proportional to the shape diameter), i.e., is  $O(n^2 \log n + n^{3/2})$ . SA has the same complexity as FMM. SSG traces all geodesics for a point in parallel. As we have more GPU cores than  $M$  directions, GPU SSG is  $O(n^{3/2})$ .

**Accuracy.** All the above methods, except SE, compute approximate geodesics. The starting angle sampling  $M$  (Section 5.2) means that SSG may miss very narrow surface dents falling between two consecutive paths  $\gamma_{S,i}$  and  $\gamma_{S,i+1}$ , i.e., may overestimate SSG length. Overestimation is not an issue for skeleton regularization: Long geodesics yield high-importance points which are to be kept anyway (red points, Fig. 6). Short geodesics, caused by surface noise which we want to eliminate by importance thresholding (blue points, Fig. 6), allow only much narrower concavities to fall between them, and thus are less affected by length overestimation.

Fig. 7 and Table 4 show the median relative error of SSG geodesic-lengths (for different  $M$  values), FMM, and SE. We used downsampled versions of *bird* and *pig* (11,718 and 3,522 points, respectively) since SE is extremely slow. SSG is more accurate than FMM for  $M > 10$ , both for median and maximum errors. For  $M = 100$ , SSG gets practically exact geodesics at a tiny cost *versus* SE. Comparing median errors with SA, SSG is more accurate for  $M \geq 30$ , see [68, Table 1] where an upper relative error bound of 0.1 percent is used. This is equivalent to SSG with  $M = 10$  directions for *bird* and  $M = 30$  directions for *pig*. As mentioned, the cost of SA is the same as FMM, i.e., hundreds of times slower than SSG.

**Memory.** For a *single* geodesic tracing on an  $n$  vertex model, Dijkstra with  $A^*$  is  $O(n)$ , FMM is  $O(n \log n)$ , Surazhky et al. is  $O(n^{3/2})$ . SSG is  $O(M)$ . Verma and Snoeyink improved upon Surazhky et al. by combining Dijkstra with  $A^*$  with the original method [73]. This reduces the memory cost to  $O(n)$ , yields a speed-up of 8, but overestimates geodesic lengths by 10 percent on average. Concluding, our GPU SSG method is a good tradeoff: It is nearly as accurate as exact geodesics, and is hundreds of times faster than approximate geodesic methods.

## 6 SURFACE SKELETON RECONSTRUCTION

Shape comparison, topological analysis, or segmentation tasks require a mesh skeleton, not a point cloud.

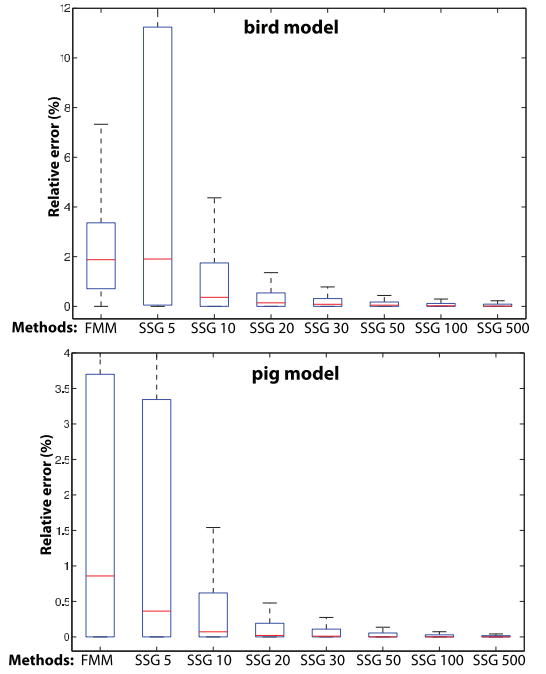


Fig. 7. Accuracy comparison: FMM *versus* SSG geodesic tracing (see Section 5.3).

Three-dimensional skeletons contain many self-intersecting, closely spaced manifolds whose boundaries are the skeleton end-curves and Y-intersection curves. Hence, point cloud reconstruction methods for locally smooth and/or nonintersecting and/or watertight surfaces cannot be used [2], [19], [34]. Reconstruction of open, nonmanifold, and self-intersecting surfaces [13], [75] is relatively slow and nontrivial. We present the next two methods for reconstructing *skeleton* surfaces from point clouds based on specific skeleton properties.

**Delaunay reconstruction.** For each triangle  $F = \{f_i\} \subset \partial\Omega$ , we use  $FT^{-1}$ , the inverse of the feature transform computed at skeleton extraction (Section 3) to gather all skeleton points  $S(F)$  having  $f_i$  as feature points. Obtaining  $FT^{-1}$  is free: For each skeleton point  $s$  found by the ball-shrinking algorithm in Section 3, the ball shrinking also gives us its two feature points  $f_1$  and  $f_2$ . By adding  $s$  to the shape points  $f_1$  and  $f_2$ , we obtain  $FT^{-1}$  at the end of the ball shrinking, i.e., for any shape point  $p \in \partial\Omega$ , all its skeleton points  $s \in S(\Omega)$ .

TABLE 4  
Accuracy and Timing Comparison for Geodesic Tracing Methods (FMM, SE, and SSG for Different Numbers of Directions  $M$ )

Method	Relative error (%)		Timing (seconds)	
	Bird	Pig	Bird	Pig
Surazhsky-exact	0	0	11209	426.2
FMM	1.87	0.85	339.6	20.9
SSG ( $M = 5$ )	1.90	0.36	0.28	0.05
SSG ( $M = 10$ )	0.36	0.07	0.56	0.08
SSG ( $M = 20$ )	0.14	0.02	1.04	0.14
SSG ( $M = 30$ )	0.08	0.009	1.54	0.22
SSG ( $M = 50$ )	0.04	$8 \cdot 10^{-4}$	2.43	0.32
SSG ( $M = 100$ )	0.02	$2 \cdot 10^{-4}$	4.83	0.62
SSG ( $M = 500$ )	0.01	$4 \cdot 10^{-5}$	23.24	2.95



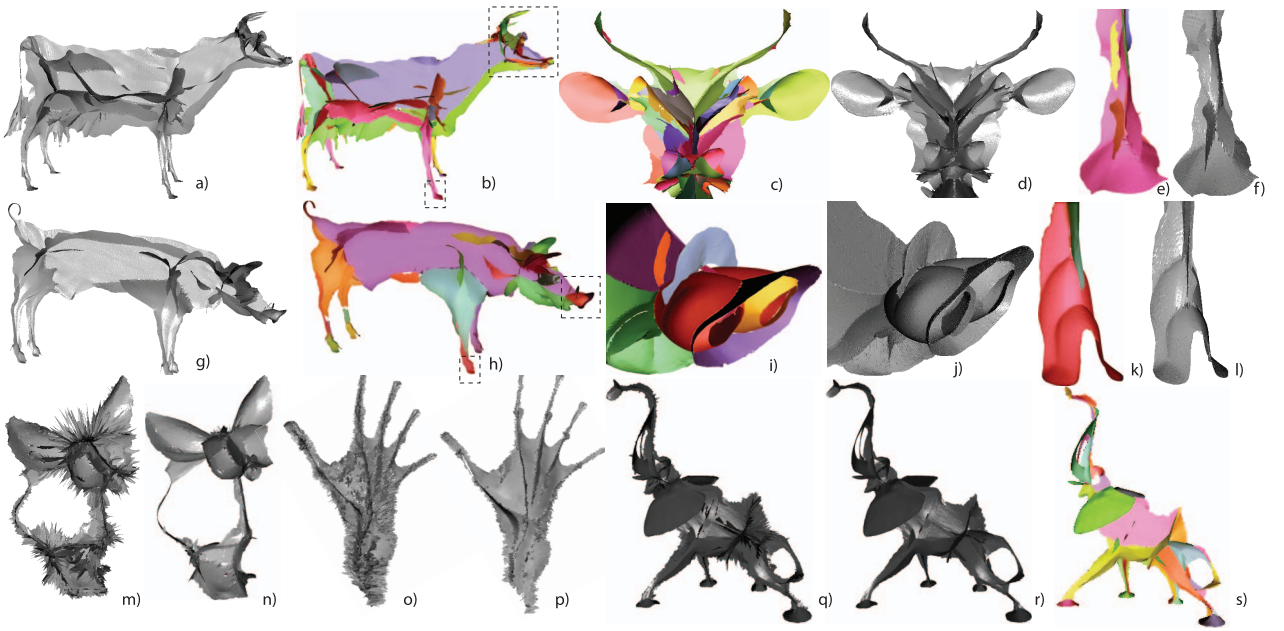


Fig. 8. Delaunay method (a), (g); details d,f,j,i; simplified clouds (m-r) and per-manifold method (b), (h), (s); details (c), (e), (i), (k) for skeleton reconstruction (Section 6).

Next, we project all points in  $S(F)$  on the plane of  $F$ , triangulate these projections [59], and use the resulting mesh patch to connect the points in  $S(F)$ . The reason for “lifting” the connectivity from 2D into 3D is that locally planar surface patches (i.e., triangles  $F$ ) create, by definition, locally planar skeleton patches (i.e., triangulation of  $S(F)$ ). This creates duplicate skeleton-mesh triangles since close model faces have common skeleton points in convex areas. To remove these, we mark all model vertices which map via the FT only to *internal* triangles, i.e., which do not have edges on the boundary of a Delaunay triangulation [59], and skip faces having only marked vertices. The method is  $O(N)$  for  $N$  skeleton points since we triangulate small point sets  $S(F)$  of size  $O(1)$ . This takes under 3 seconds for all shapes in this paper. We use only *local* information (skeleton points of a small surface neighborhood), so we can do out-of-core reconstruction of large skeletons, like [13].

Figs. 8 and 9 show our results. All small details (cow eyes, hooves, horns, and pig snout) create skeletal manifolds. Noisy skeletons have no “stitches” between close ligature sheets (Figs. 8m, 8o, and 8q). It is challenging to reconstruct such manifolds *only* from point clouds: Ligatures match surface concavity pairs [50], so their cloud density can be arbitrarily small even for densely sampled models (Section 3). The inverse FT links ligatures to the input surface and thus reconstructs them well. Simplified skeleton meshes are easily created by filtering low-importance points (compare Figs. 8n, 8p, and 8r to the raw skeletons in Figs. 8m, 8o, and 8q).

**Permanifold reconstruction.** The Delaunay method leaves a few tiny holes in the skeleton mesh (Figs. 8d, 8f, 8j, and 8l). Our second reconstruction method fixes these. First, we cluster skeleton points into separate manifolds. For this, we observe that a small ball  $\nu_\varepsilon(s) \subset S$  of radius  $\varepsilon$  around a skeleton point  $s$  maps to one or more small vicinities  $\nu_{\partial\Omega}^i(s)$  of the input shape [50]. Points on the manifold end-curves,

inside a manifold, and on Y-intersection curves have one, two, and three or more  $\nu_{\partial\Omega}^i$ , respectively. We cluster skeleton points into manifolds by a simple flood fill which groups adjacent vicinities  $\nu_\varepsilon(s)$  having average feature vectors that differ less than an angle  $\alpha$  (in practice,  $\alpha = 5^\circ$ ). The fill stops when we find a vicinity with a highly different feature vector, i.e., at Y-intersection curves. We repeat the fill from a random unclustered point until all points are clustered. Finally, we reconstruct each cluster with the ball pivoting algorithm (BPA) [8] with ball radius  $\rho_{ball}$  set to the average interpoint distance in the cluster. BPA incrementally grows a triangle mesh surface as follows: Starting with a seed triangle, a ball of a given size  $\rho_{ball}$  pivots around each triangle edge ( $e_1, e_2$ ), i.e., revolves around the edge while keeping contact with the edge’s

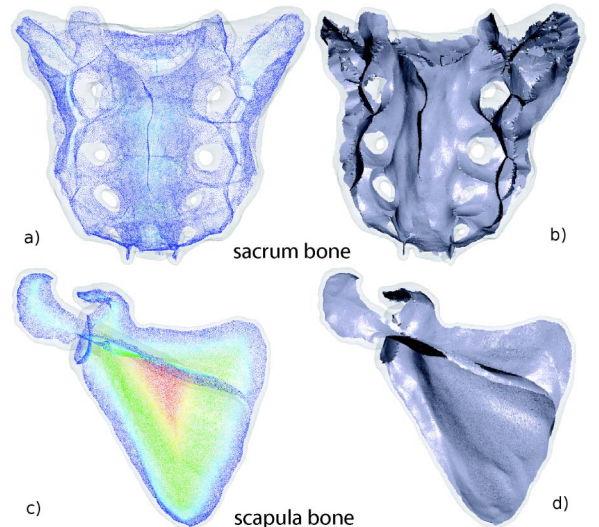


Fig. 9. Anatomic shapes: point clouds (a), (c) and surface skeletons (b), (d).

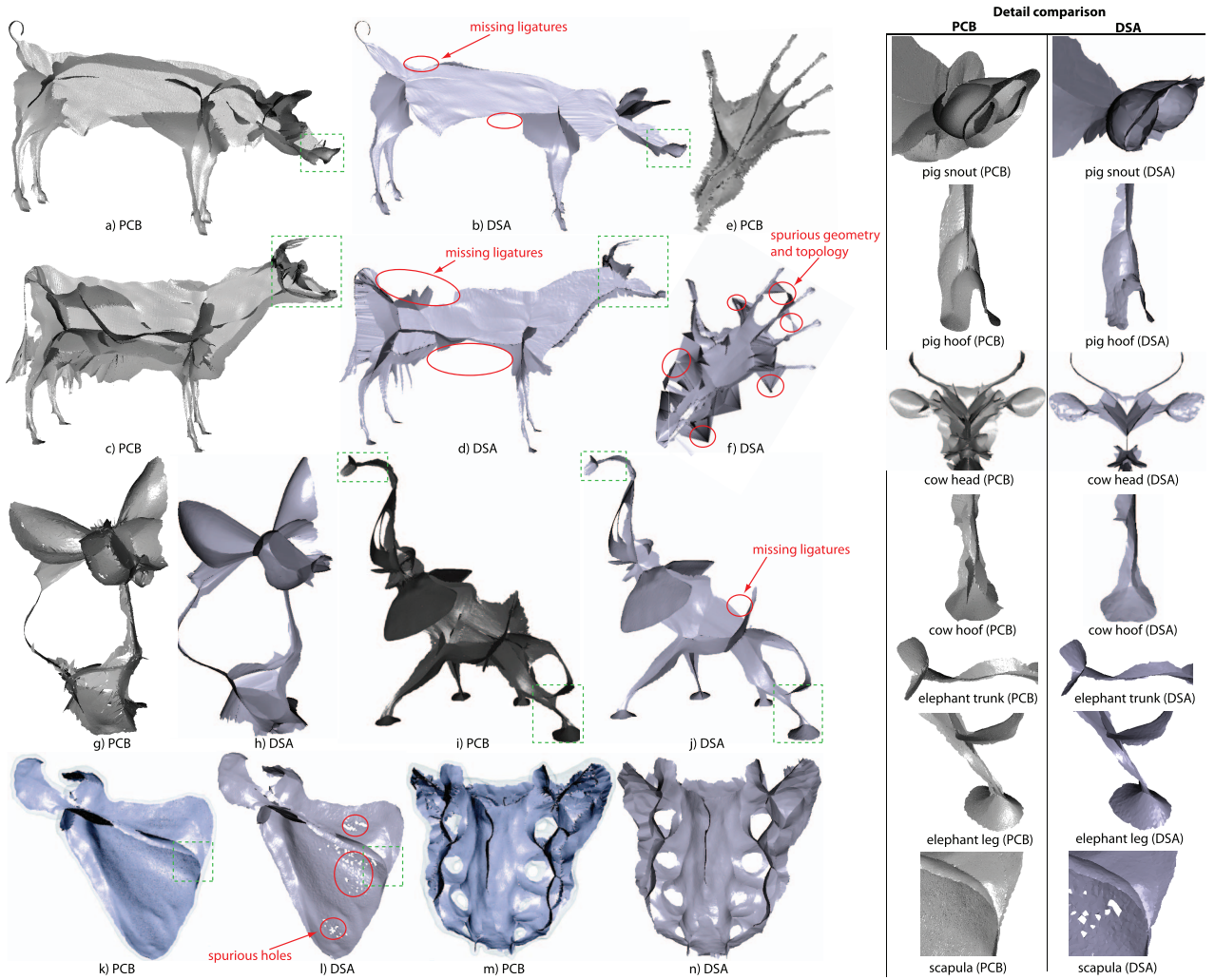


Fig. 10. Comparison of PCS and DSA methods (Section 7). Skeleton parts wrongly added/missed by DSA are marked red. Green-marked details are shown right.

endpoints, until it touches a point  $p$  from our point-cluster, and without containing any other cluster point except  $p$  and the edge's endpoints. When  $p$  is found, a new triangle  $(p, e_1, e_2)$  is added to the mesh. The process is repeated from the edges of the newly found triangle until all possible edges have been considered. For full details, we refer to [8] and to the public MeshLab implementation of BPA we have used here [42].

Figs. 8b, 8h, and 8s show results, with manifolds colored differently for illustration. Per-manifold reconstruction removes the small holes and intermanifold stitches at Y-intersection curves of the Delaunay method (compare Figs. 8c, 8e, 8i, and 8k and Figs. 8d 8f, 8j, and 8l) at a higher execution time: 12 seconds for the cow and pig models.

## 7 SURFACE SKELETON COMPARISON

We compare our point-cloud surface skeletons (PCS) with the discrete scale axis (DSA) method [43], one of the best methods for extracting detailed surface skeletons (Fig. 10). For similar skeleton simplification levels, PCS and DSA create similar skeletons (Figs. 10g, 10h, 10m, and 10n). Yet, differences exist (Fig. 10, red marks). These have two

causes: geometry (different skeleton points found) and topology (same skeleton points found but connected differently). Geometry differences imply topology differences. Note how DSA found many skeleton points outside the hand model (Figs. 10e and 10f) and connected these to points inside the hand. In the cow model (Figs. 10c and 10d), skeleton points are largely identical, but DSA wrongly connects the tail and rump skeletons. Such issues, due to strong model concavities, are noted in [43].

DSA can skip large parts of the skeleton periphery, see, e.g., the pig and cow spine and belly and elephant spine (Figs. 10b, 10d, and 10j). These parts, found by our PCS, are *ligature* sheets between the core skeleton and faraway skeleton points in shallow surface cusps [50]. The reason hereof is that PCS and DSA use different skeleton *scale* metrics: PCS uses geodesic importance (a global metric); DSA computes simplified skeletons by up-scaling the input shape (a local operation). DSA also creates many small holes in skeletal sheets, see Fig. 10l. These artifacts (for a genus 0 shape) are likely due to the numerical degeneracies listed in [43].

Table 5 shows timing and size statistics for PCS and DSA. For PCS, we used an accuracy  $\tau = 10^{-3}$  (Section 3),



TABLE 5  
Timing Comparison of PCS and DSA Skeletonization Methods

Model	PCS (our method)		DSA(Miklos <i>et al.</i> [43])		
	time (sec.)	points	time (sec.) $\delta = 0.007$	time (sec.) $\delta = 0.005$	points
pig	27.9	224539	485	975	145153
cow	19.4	185703	448	919	64240
bird	3.3	46862	201	421	104140
horse	17.5	193887	369	744	63297
asiandragon	14.9	230964	n/a	n/a	n/a
hand	4.8	196920	378	778	93301
elephant	3.5	50422	505	1031	166089
armadillo	13.2	172955	426	853	105167

and also added regularization time. For DSA, we used approximation thresholds  $\delta$  for the mesh to union-of-balls conversion of 0.007 and 0.005 ([43], Section 2). Note that  $\tau = 10^{-3}$  for PCS is similar to  $\delta = 10^{-3}$  for DSA as for skeleton accuracy. PCS is up to 100 times faster than DSA. More accurate UoB settings (smaller  $\delta$ ) make DSA much slower: 45 minutes for a 313K-point skeleton of a 177K-triangle shape at  $\delta = 0.002$  [43]. We could not test such settings as  $\delta \leq 0.003$  made DSA crash on our models. The same was true for the asiandragon model,  $\delta = 0.007$ . If we replace our SSG regularization by simpler metrics, e.g.,  $\theta$ -SMA, PCS becomes much faster, basically identical to the timings in Table 1.

PCS and DSA create skeletons of different sizes. PCS creates one skeleton point per input point (Section 3). DSA uses a Voronoi diagram, which has a different point count. Yet, the skeletal *detail* created by PCS is similar to DSA (see Fig. 10).

We also compared PCS with the method of Stolpner *et al.* [64] which approximate medial axes as UoB point clouds. On a 3.4 GHz PC, PCS is over 100 times faster (Table 5 *versus* Table 1 [64]).

## 8 CURVE SKELETON EXTRACTION

Curve skeleton points are surface skeleton points which have two or more SSGs between their feature points [20], [55]. The above definition for curve skeleton points can be quite easily applied to detect such points for voxel-based models, as shown in [55]. For surface skeletons represented as point clouds, as in our case, the above criterion cannot be immediately used, mainly due to the typically nonuniform density of skeleton point clouds (see Section 3.1). Therefore, we propose to extract curve skeletons by a method akin to the technique of Siddiqi *et al.* [60], [61]. Our proposal is based on the following observation: In a small vicinity  $\mathcal{N}$  of a curve-skeleton point, geodesic tangents, mapped to  $\mathcal{N}$ , abruptly change directions (Fig. 11). Given this observation, we extract curve-skeleton points by looking for high-response points of weight-averaged tangent directions in vicinities around each surface-skeleton point by a three-step method: 1) Find candidates close to the curve skeleton; 2) filter and regularize candidates; and 3) reconstruct the curve skeleton.

### 8.1 Detecting Candidate Curve Skeleton Points

For each surface skeleton point  $s_i$ , we compute the average (projected) tangent direction of its SSG path, i.e.,

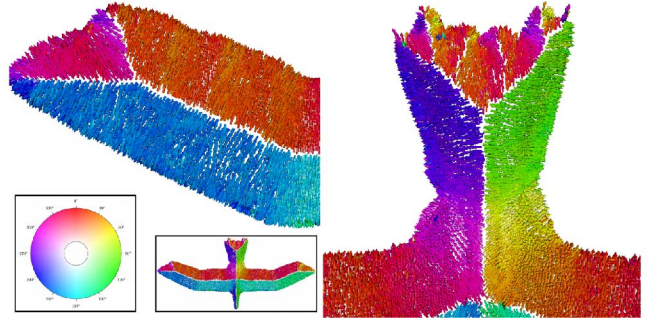


Fig. 11. Tangent vector field  $\mathbf{T}$  (shown with directional color-coding).

$$\begin{aligned} \mathbf{t}'_{s,i} &= \mathbf{t}_{s,i} - \mathbf{f}_i(\mathbf{f}_i \cdot \mathbf{t}_{s,i}), \\ \mathbf{t}'_{e,i} &= \mathbf{t}_{e,i} - \mathbf{f}_i(\mathbf{f}_i \cdot \mathbf{t}_{e,i}), \\ \mathbf{t}_i &= \frac{\mathbf{t}'_{s,i} + \mathbf{t}'_{e,i}}{\|\mathbf{t}'_{s,i} + \mathbf{t}'_{e,i}\|}, \end{aligned} \quad (4)$$

where  $\mathbf{t}_{s,i}$  and  $\mathbf{t}_{e,i}$  are the tangent vectors at its feature points, and  $\mathbf{f}_i$  is the normalized feature vector of  $s_i$ . Projection improves the detector reliability (see below) close to Y-intersection curves, i.e., where several skeletal manifolds intersect [18].

Tangent vectors  $\mathbf{t}_i$  span a vector field  $\mathbf{T}$  over the surface skeleton (Fig. 11).

One can evaluate the divergence of  $\mathbf{T}$  or its more numerically stable flux [60]. Points close to the curve skeleton have large positive flux/divergence values. However, along with these, this approach may yield also points close to the Y-intersection curves.

We find candidate curve-skeleton points differently. For each skeleton point  $s_i$ , let  $\mathcal{N}_i$  be its set of neighbor skeleton points (we use 10 nearest neighbors in practice). We measure the likelihood of  $s_i$  being a curve-skeleton point as

$$I(s_i) = \rho_i - \rho_i \left\| \frac{\sum_{j \in \mathcal{N}_i} w_{ij} \mathbf{t}_j}{\sum_{j \in \mathcal{N}_i} w_{ij}} \right\|, \quad w_{ij} = |\mathbf{f}_i \cdot \mathbf{f}_j| e^{-\frac{(\rho_i - \rho_j)^2}{2\sigma_1^2} - \frac{\|\mathbf{s}_i - \mathbf{s}_j\|^2}{2\sigma_2^2}},$$

with  $\rho_i \equiv \rho(s_i)$ . The importance  $I_i \equiv I(s_i)$  averages tangent vectors in  $\mathcal{N}_i$  with weights given by a 2D Gaussian kernel and  $\sigma_1, \sigma_2$  set to the median of the distances  $\|\mathbf{s}_i - \mathbf{s}_j\|_{j \in \mathcal{N}_i}$ . The weight  $w_{ij}$  lowers the impact of tangent vectors  $\mathbf{t}_j$  of skeleton points  $s_j$  which: 1) have feature vectors  $\mathbf{f}_j$  not parallel to  $\mathbf{f}_i$ , 2) have geodesics of different lengths (following [20], [55]), and 3) are far from  $s_i$ . Points close to Y-intersection curves meet conditions 1) and 2), so they contribute weakly to  $I$ . In contrast, points close to the curve skeleton yield large weights, and have tangent vectors pointing outward in all directions (see Fig. 11). Such points have large  $I$  values, so we find the set  $\mathcal{C}$  of candidate curve-skeleton points by thresholding  $I$  at a small value  $T_I > 0$ .

### 8.2 Regularization of Candidate Curve-Skeleton Points

We assign an importance  $\mu_i$  to each point  $s_i \in \mathcal{C}$  to prune spurious curve skeleton details. We set  $\mu_i$  to the smallest surface area between two SSGs of *nearby* skeleton points. This is similar to the metric in [55], which was computed by a flood-fill on a voxel surface. Our case is more complicated as we have two curves on an unstructured *mesh*. We

efficiently *approximate* this area using only the angle between the two geodesics and the lengths of a few additional straightest geodesics as follows.

For each candidate  $s_i \in \mathcal{C}$ , we find a neighbor  $j^* \in \mathcal{M}_i$ , with  $\mathcal{M}_i$  a neighborhood of  $s_i$  (10 nearest neighbors), for which

$$J_j = (1 + \mathbf{t}_i \cdot \mathbf{t}_j) e^{-\frac{(t_i - t_j)^2}{2\sigma_1^2} - \frac{\|\mathbf{s}_i - \mathbf{s}_j\|^2}{2\sigma_2^2}}, \quad (5)$$

is minimal, i.e.,  $j^* = \operatorname{argmin}_{j \in \mathcal{M}_i} J_j$ . Since  $s_i$  and  $s_{j^*}$  are spatially close, we assume that their feature points coincide, and use  $s_i$  for these. Let  $\theta = \angle(\mathbf{t}_i, \mathbf{t}_{j^*}) \in [0, \pi]$  be the angle between the tangent vectors of  $s_i$  and  $s_{j^*}$ . The pair of SSGs  $\gamma_{se,i}$  and  $\gamma_{se,j^*}$  between the feature points  $\mathbf{f}_{1,i}$  and  $\mathbf{f}_{2,i}$  divide the surface  $\partial\Omega$  into two parts, the smallest area of which we want to estimate. For this, we trace  $P$  straightest geodesics  $\gamma_{S,i,k}$ ,  $1 \leq k \leq P$ , from  $\mathbf{f}_{1,i}$  to  $\mathbf{f}_{2,i}$  on  $\partial\Omega$ , with uniformly spread starting angles  $\alpha_k = 2\pi k/P$  around the vector  $\mathbf{f}_i = \mathbf{f}_{1,i} - \mathbf{f}_{2,i}$  at  $\mathbf{f}_{1,i}$ . Assuming that each geodesic is half of an *ellipse*, with minor axis  $\mathbf{f}_i$ , the ellipse radii  $a_k$  and  $b_k \geq a_k$  are given by a simple approximation formula for an ellipse perimeter, i.e.,  $a_k = \|\mathbf{f}_i\|/2$  and  $b_k = (2 \|\gamma_{S,i,k}\| - \pi a_k)/2$ . Next, we approximate  $\partial\Omega$  between two consecutive geodesics by an *oblate spheroid* with radii  $a_k$  and  $c_k = (b_k + b_{k+1})/2$ , so its area is that of an oblate spheroid wedge with angle  $\beta = 2\pi/P$ , i.e.,

$$S_k = \beta c_k^2 + \frac{\beta a_k^2}{2e} \ln \frac{1+e}{1-e}, \quad (6)$$

with  $e = \sqrt{1 - a_k^2/c_k^2}$ . Assuming that the starting direction  $\alpha_0 = 0$  corresponds to the tangent of  $\gamma_{se,i}$ , we compute  $\mu_i$  as

$$\mu_i = \min \left( \sum_{k, \alpha_k < \theta} S_k, \sum_{k, \alpha_k \geq \theta} S_k \right). \quad (7)$$

Thresholding  $\mu$  removes short curve-skeleton branches to yield the final candidate set  $\mathcal{C}'$ . We use more paths  $P = 50$  than for the surface skeleton metric ( $M = 20$ , Section 5) to limit area estimation errors.  $\sigma_1$  and  $\sigma_2$  are set to the median distance in  $\mathcal{M}_i$ .

### 8.3 Curve Skeleton Reconstruction

To get the final curve skeleton  $CS$ , we connect points in  $\mathcal{C}'$  by line segments by adapting the ball-pivoting method [8]. We start from the point with largest importance  $\max_{\mathcal{C}'}(\mu)$ , find its neighbor in  $\mathcal{C}'$  within a radius  $r$  with largest  $\mu$  value, and add a new line segment to  $CS$ . Next, we try to extend  $CS$  by searching neighbors of its end vertices  $\mathbf{e}_i$ . To become a new end vertex, a point  $\mathbf{x}$  must 1) be within distance  $r$  from an  $\mathbf{e}_i$ , and 2) the segment  $(\mathbf{x}, \mathbf{e}_i)$  must be well aligned with the curve tangent. When  $CS$  cannot be extended, we backtrack and try to extend from vertices of previous segments. This captures the curve skeleton branching.

### 8.4 Comparison

Regularization (Section 8.2) is the costliest step of our curve-skeleton extraction.  $\mathcal{C}$  is a small subset of the surface skeleton, but tracing  $P = 50$  straightest geodesics  $\gamma_{S,i,k}$  per point  $s_i \in \mathcal{C}$  is still expensive as no early termination can be used (Section 5). Still, we only need to compute geodesic lengths. This results in a very efficient CUDA mapping (see Table 6).

TABLE 6  
Curve-Skeleton Extraction Timings

Model	Detect (seconds)	Regularize (seconds)	Reconstruct (seconds)	Total (seconds)
Cow	3.1	3.5	0.8	7.4
Bird	0.5	1.2	0.1	1.8
Horse	2.5	2.6	0.2	5.3
Asiandragon	2.6	3.7	1.7	8.0
Hand	1.3	1.9	0.6	3.8
Elephant	0.5	1.5	0.5	2.5
Buddha	3.3	5.3	0.8	9.4
Mouse	3.0	4.6	0.9	8.5
Dragon	3.5	4.7	0.9	9.1
Pig	2.5	4.0	0.8	7.3
Armadillo	1.8	1.5	0.6	3.9
Rabbit	0.5	1.1	0.5	2.1

Fig. 12 compares our results with Reniers et al. [55] and with that of Au et al. who compute curve-skeletons by shape collapse via Laplacian smoothing [5]. Although our point count is smaller than, or at most equal to, the surface voxel count of Reniers et al., we find more skeleton branches, e.g., the cow udder and horns. Our skeletons, unlike Au et al., do not have artificial straight-line branches and sharp bends. Au et al. added these in a “surgery” step to connect disjoint skeleton parts (see green markers, hand and horse model, Fig. 12 bottom). The skeletons of Au et al. extend deeper into surface cusps, e.g., the pig’s hooves and snout. Such branches are shortened by our regularization (Section 8.2). Our method is, on average, 50 times faster than Au et al. and over one order of magnitude faster than Reniers et al. Interestingly, the costs of the latter two are similar since both methods “visit” the entire input volume: Au et al. while collapsing the mesh and Reniers et al. while computing its voxel skeleton detectors.

### 8.5 Relation to Surface Skeletons

As stated at the beginning of Section 8, we detect curve skeleton points as a subset of surface skeleton points, so our curve skeleton is always a subset of the corresponding surface skeleton point-cloud. Both curve and surface skeletons can be simplified (regularized), and the relation between these two regularization types is as follows: First, we can regularize a surface skeleton using the SSG-length importance metric  $\rho$  (Section 5), and then compute the curve skeleton of the regularized surface skeleton. This approach, however, may eliminate entire curve-skeleton terminal branches, which correspond to thin and narrow shape parts, such as the pig’s tail or cow’s horns in Fig. 12, since the surface skeleton has a low importance in such regions. Alternatively, we can extract the curve skeleton from the full surface skeleton, and regularize the former by thresholding its own importance  $\mu$  (7). This has the advantage of simplifying curve-skeleton terminal branches more uniformly.

A mixed curve-and-surface skeleton can be easily extracted too. For this, we replace the importance  $\rho$  of the surface skeleton points which have been detected to be also on the curve skeleton by the corresponding curve skeleton importance  $\mu$ . Note that, for all curve skeleton points  $\mathbf{p} \in CS$ ,  $\mu(\mathbf{p}) > \rho(\mathbf{p})$  since the former measures an area whose boundary length is the latter. Given this, and as already shown for the voxel case in [55], thresholding  $\rho$  with



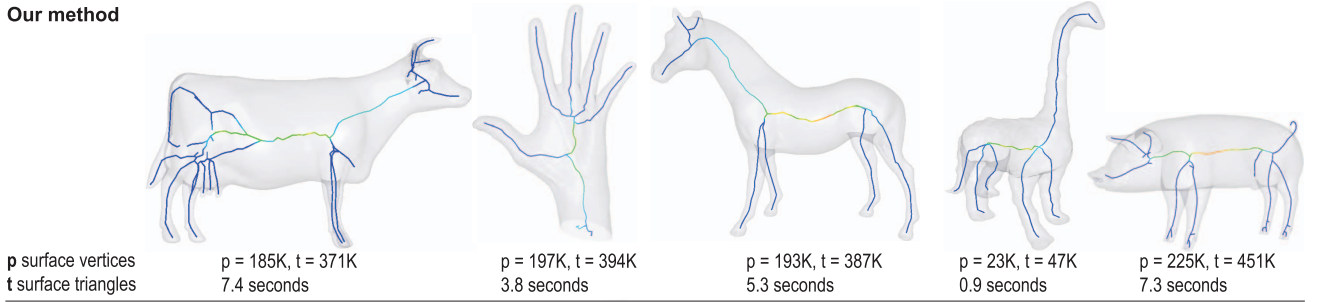
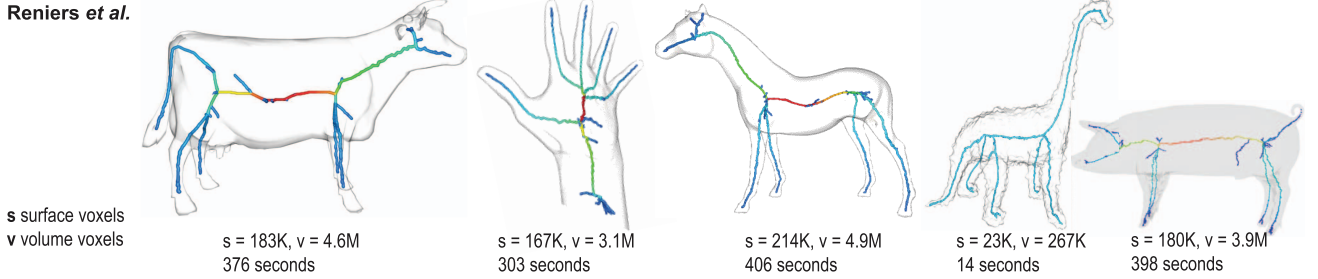
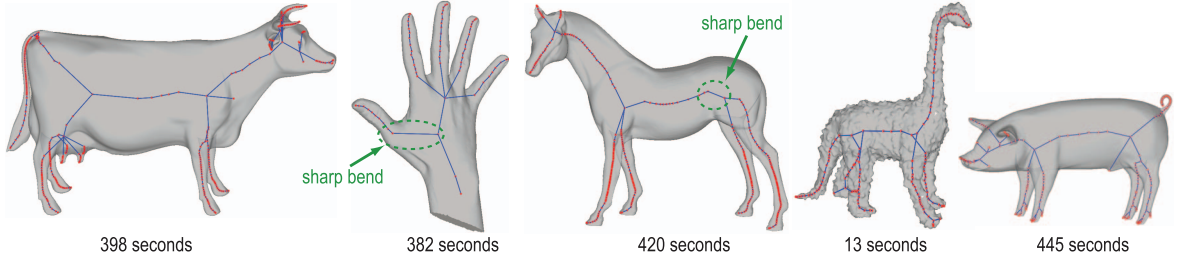
**Our method****Reniers et al.****Au et al.**

Fig. 12. Curve skeleton extraction: Our method (top row), voxel-based method [55] (middle row), and mesh collapse method [5] (bottom row).

increasing values will now deliver a mixed curve-and-surface skeleton, where the surface skeleton is first progressively simplified toward the curve skeleton, followed by the simplification of the higher importance curve skeleton.

## 9 DISCUSSION

We next discuss our framework *versus* several related methods.

**Input.** We use (nonuniform) mesh models instead of voxel models. Our input can be of any genus (see the rabbit, cat, and dragon models), self-intersecting (cow model), and nonclosed (hand model). Skeleton extraction and shape rendering only require an oriented point cloud input. We need connectivity data only for the regularization and Delaunay-based reconstruction.

**Accuracy.** Voxel-based skeletons are limited by the voxel resolution [11], [31], [55]. Like Stolpner et al. [64], our skeletons are point clouds close to the true medial axis within a user-prescribed precision in world space. Our image-based shape reconstruction from its (simplified) skeleton is real-time and near-pixel accurate.

**Scalability.** A  $1,024^3$  distance-and-feature-transform volume needs at least 4 GB RAM [11], [30], [70]. An equivalent mesh, roughly 1 M triangles, needs only 24 MB RAM, which is essential for typical 1 GB GPU RAM limits. Voxelization also has large speed costs and is delicate for certain meshes [23], [24], [46]. Multiresolution voxel schemes reduce memory costs but complicate algorithms

and reduce GPU speedups. Table 1 (Section 3) ( $\tau = 10^{-3}$ ,  $\varepsilon = 0$ , equivalent to a  $1,024^3$  volume) shows that our method is over 100 times faster than [10], [20], [37], [43], [55], [64], even without voxelization.

**Geodesic computation.** Our GPU computation of shortest, straightest geodesics is over two orders of magnitude faster, and more accurate, than state-of-the-art techniques [49], [68], [73]. This makes global skeleton regularization practical for large models. Our SSG method is also usable for other applications requiring fast, near-exact, geodesics on meshes.

**Simplicity.** Our framework has no complex computational geometry operations or degenerate cases, unlike [43], [55], [64]. Its only user parameters are the skeleton centeredness  $\tau$  and number of geodesic directions  $M$ , explained in Sections 3 and 5.

**Curve skeletons.** Existing *curve* skeleton extractors have widely different speed, accuracy, and curve skeleton definitions [5], [14], [15], [20], [30]. Our curve skeletons cannot replace all such methods. Our main novelty is the fast extraction of curve skeletons from a *surface* skeleton cloud. The closest methods to ours are the medial geodesic function [20] and ROSA [69]. Yet, we use a different angle-based criterion than MGF and also than ROSA, which computes curve skeletons as centers of point cloud projections on a cut plane found by optimizing for circularity. We are two orders of magnitude faster than ROSA and MGF, and on average 50 times faster than Au et al. [5] (Section 8.3). Compared to the variational method

of Hassouna and Farag [30], we are 20 times faster (Fig. 12 and Table 6 versus [30, Fig. 10]).

## 10 CONCLUSION

We have presented a GPU-based framework for extracting surface and curve skeletons from large meshes. Using GPUs to parallelize several extraction steps (maximal ball computation, regularization, and surface reconstruction), we obtain similar or higher quality surface and curve skeletons with two orders of magnitude speed-up over state-of-the-art methods. Skeleton clouds, extracted with user-desired accuracy, are regularized by a new parallel computation of shortest, straightest geodesics which is over two orders of magnitude faster, and more accurate, than similar schemes. From the skeleton cloud, we reconstruct the input shapes in real-time by an image-based method or extract high-quality mesh and curve skeletons for further use in applications such as shape analysis, classification, and matching.

## REFERENCES

- [1] N. Ahuja and J. Chuang, "Shape Representation Using a Generalized Potential Field Model," *IEEE Trans. Pattern Analysis and Machine Intelligence*, vol. 19, no. 2, pp. 169-176, Feb. 1997.
- [2] N. Amenta, S. Choi, T.K. Dey, and N. Leekha, "A Simple Algorithm for Homeomorphic Surface Reconstruction," *Int'l J. Computational Geometry Applications*, vol. 12, pp. 125-141, 2002.
- [3] N. Amenta, S. Choi, and R. Kolluri, "The Power Crust," *Proc. Sixth ACM Symp. Solid Modeling and Applications*, pp. 65-73, 2001.
- [4] C. Aslan, A. Erdem, E. Erdem, and S. Tari, "Disconnected Skeleton: Shape at Its Absolute Scale," *IEEE Trans. Pattern Analysis and Machine Intelligence*, vol. 30, no. 12, pp. 2188-2203, Dec. 2008.
- [5] O.K.C. Au, C. Tai, H. Chu, D. Cohen-Or, and T. Lee, "Skeleton Extraction by Mesh Contraction," *Proc. ACM Siggraph*, pp. 441-449, 2008.
- [6] X. Bai and L. Latecki, "Path Similarity Skeleton Graph Matching," *IEEE Trans. Pattern Analysis and Machine Intelligence*, vol. 30, no. 7, pp. 1282-1292, July 2008.
- [7] X. Bai, L. Latecki, and W.-Y. Liu, "Skeleton Pruning by Contour Partitioning with Discrete Curve Evolution," *IEEE Trans. Pattern Analysis and Machine Intelligence*, vol. 29, no. 3, pp. 449-462, Mar. 2007.
- [8] F. Bernardini, J. Mittleman, H. Rushmeier, C. Silva, and G. Taubin, "The Ball-Pivoting Algorithm for Surface Reconstruction," *IEEE Trans. Visualization and Computer Graphics*, vol. 5, no. 4, pp. 349-359, Oct-Dec. 1999.
- [9] S. Bouix, K. Siddiqi, and A. Tannenbaum, "Flux Driven Automatic Centerline Extraction," *Medical Image Analysis*, vol. 9, no. 3, pp. 209-221, 2005.
- [10] S. Bouix, K. Siddiqi, A. Tannenbaum, and S. Zucker, "Medial Axis Computation and Evolution," *Statistics and Analysis of Shape*, pp. 1-28, 2006.
- [11] T. Cao, K. Tang, A. Mohamed, and T. Tan, "Parallel Banding Algorithm to Compute Exact Distance Transform with the GPU," *Proc. Siggraph Symp. Interactive 3D Graphics*, pp. 134-141, 2010.
- [12] L. Cayton, "A Nearest Neighbor Data Structure for Graphics Hardware," *Proc. Advanced Distribution Management System Conf.*, pp. 192-197, people.kyb.tuebingen.mpg.de/lcayton, 2010.
- [13] M. Chang, F. Leymarie, and B. Kimia, "Surface Reconstruction from Point Clouds by Transforming the Medial Scaffold," *Computer Vision and Image Understanding*, vol. 113, pp. 1130-1146, 2009.
- [14] J. Chuang, C. Tsai, and M. Ko, "Skeletonization of Three-Dimensional Object Using Generalized Potential Field," *IEEE Trans. Pattern Analysis and Machine Intelligence*, vol. 22, no. 11, pp. 1241-1251, Nov. 2000.
- [15] N. Cornea, D. Silver, and P. Min, "Curve-Skeleton Properties, Applications, and Algorithms," *IEEE Trans. Visualization and Computer Graphics*, vol. 13, no. 3, pp. 87-95, May/June 2007.
- [16] N. Cornea, D. Silver, X. Yuan, and R. Balasubramanian, "Computing Hierarchical Curve-Skeletons of 3D Objects," *Visual Computer*, vol. 21, no. 11, pp. 945-955, 2005.
- [17] L. Costa and R. Cesar, *Shape Analysis and Classification*. CRC Press, 2000.
- [18] J. Damon, "Global Medial Structure of Regions in  $\mathbb{R}^3$ ," *Geometry and Topology*, vol. 10, pp. 2385-2429, 2006.
- [19] T. Dey and S. Goswami, "Provable Surface Reconstruction from Noisy Samples," *Int'l J. Computational Geometry and Applications*, vol. 35, no. 1, pp. 340-355, 2006.
- [20] T. Dey and J. Sun, "Defining and Computing Curve Skeletons with Medial Geodesic Functions," *Proc. Fourth Eurographics Symp. Geometry Processing*, pp. 143-152, 2006.
- [21] T. Dey and W. Zhao, "Approximating the Medial Axis from the Voronoi Diagram with a Convergence Guarantee," *Algorithmica*, vol. 38, pp. 179-200, 2003.
- [22] R. Dougherty and K. Kunzelmann, "Computing Local Thickness of 3D Structures with ImageJ," *Microscopy and Microanalysis*, vol. 12, pp. 1678-1679, www.optnav.com/LocalThicknessEd.pdf, 2007.
- [23] E. Eisemann and X. Decoret, "Fast Scene Voxelization and Applications," *Proc. Siggraph Symp. Interactive 3D Graphics*, pp. 71-78, 2006.
- [24] M. Foskey, M. Lin, and D. Manocha, "Efficient Computation of a Simplified Medial Axis," *Proc. Shape Modeling Conf.*, pp. 135-142, 2003.
- [25] P. Frey, "YAMS: A Fully Automatic Adaptive Isotropic Surface Remeshing Procedure," Technical Report 0252, INRIA, www.ann.jussieu.fr/frey, Nov. 2001.
- [26] V. Garcia, E. Debreuve, and M. Barlaud, "Fast k Nearest Neighbor Search Using GPU," *Proc. Conf. Visual Computer on GPU*, pp. 77-83, 2008.
- [27] Y. Ge and J. Fitzpatrick, "On the Generation of Skeletons from Discrete Euclidean Distance Maps," *IEEE Trans. Pattern Analysis and Machine Intelligence*, vol. 18, no. 11, pp. 1055-1066, Nov. 1996.
- [28] P. Giblin and B. Kimia, "A Formal Classification of 3D Medial Axis Points and Their Local Geometry," *IEEE Trans. Pattern Analysis and Machine Intelligence*, vol. 26, no. 2, pp. 238-251, Jan. 2004.
- [29] J. Giesen, B. Miklos, M. Pauly, and C. Wormser, "The Scale Axis Transform," *Proc. 25th Ann. Symp. Computational Geometry*, pp. 106-115, 2009.
- [30] M. Hassouna and A. Farag, "Variational Curve Skeletons Using Gradient Vector Flow," *IEEE Trans. Pattern Analysis and Machine Intelligence*, vol. 31, no. 12, pp. 2257-2274, Dec. 2009.
- [31] W. Hesselink and J. Roerdink, "Euclidean Skeletons of Digital Image and Volume Data in Linear Time by the Integer Medial Axis Transform," *IEEE Trans. Pattern Analysis and Machine Intelligence*, vol. 30, no. 12, pp. 2204-2217, Dec. 2008.
- [32] I. Hotz and H. Hagen, "Visualizing Geodesics," *Proc. IEEE Visualization*, pp. 311-318, 2000.
- [33] S. Katz and A. Tal, "Hierarchical Mesh Decomposition Using Fuzzy Clustering and Cuts," *ACM Trans. Graphics*, vol. 22, no. 3, pp. 954-961, 2003.
- [34] M. Kazhdan, M. Bolitho, and H. Hoppe, "Poisson Surface Reconstruction," *Proc. Eurographics Symp. Geometry Processing*, pp. 61-70, 2006.
- [35] R. Kimmel, D. Shaked, N. Kiryati, and A. Bruckstein, "Skeletonization via Distance Maps and Level Sets," *Computer Vision and Image Understanding*, vol. 62, no. 3, pp. 382-391, 1995.
- [36] J. Lambourne, D. Bruijic, Z. Djuric, and M. Ristic, "Calculation and Visualisation of the Thickness of 3D CAD Models," *Proc. Int'l Conf. Shape Modeling and Applications*, pp. 107-112, 2005.
- [37] F. Leymarie and B. Kimia, "The Medial Scaffold of 3D Unorganized Point Clouds," *IEEE Trans. Visualization and Computer Graphics*, vol. 29, no. 2, pp. 313-330, Mar./Apr. 2007.
- [38] F. Leymarie and M. Levine, "Simulating the Grassfire Transform Using an Active Contour Model," *IEEE Trans. Pattern Analysis and Machine Intelligence*, vol. 14, no. 1, pp. 56-75, Jan. 1992.
- [39] X. Li, T. Woon, T. Tan, and Z. Huang, "Decomposing Polygon Meshes for Interactive Applications," *Proc. Symp. Interactive 3D Graphics*, pp. 35-42, 2001.
- [40] J. Ma, S.W. Bae, and S. Choi, "3D Medial Axis Point Approximation Using Nearest Neighbors and the Normal Field," *Visual Computer*, vol. 28, no. 1, pp. 7-19, 2012.
- [41] G. Malandain and S. Fernandez-Vidal, "Euclidean Skeletons," *Image and Vision Computing*, vol. 16, no. 5, pp. 317-327, 1998.

- [42] MeshLab "MeshLab Geometry Processing Software, 2012," meshlab.sourceforge.net. 2012.
- [43] B. Miklos, J. Giesen, and M. Pauly, "Discrete Scale Axis Representations for 3D Geometry," *Proc. ACM Siggraph*, pp. 394-493, 2010.
- [44] M. Mortara, G. Patanet, M. Spagnuolo, B. Falcidieno, and J. Rossignac, "Plumber: A Method for Multiscale Decomposition of 3D Shapes into Tubular Primitives and Bodies," *Proc. ACM Symp. Solid Modeling and Applications*, pp. 339-344, 2004.
- [45] D. Mount and S. Arya, "Approximate Nearest Neighbor Search Software," [www.cs.umd.edu/mount/ANN](http://www.cs.umd.edu/mount/ANN), 2011.
- [46] F. Nooruddin and G. Turk, "Simplification and Repair of Polygonal Models Using Volumetric Techniques," *IEEE Trans. Visualization and Computer Graphics*, vol. 9, no. 2, pp. 191-205, [www.cs.princeton.edu/min/binvox](http://www.cs.princeton.edu/min/binvox), Apr-June 2003.
- [47] R.L. Ogniewicz and O. Kubler, "Hierarchic Voronoi Skeletons," *Pattern Recognition*, vol. 28, pp. 343-359, 1995.
- [48] K. Palagyi and A. Kuba, "Directional 3D Thinning Using 8 Subiterations," *Proc. Eighth Int'l Conf. Discrete Geometry for Computer Imagery*, pp. 325-336, 1999.
- [49] G. Peyre and L. Cohen, "Geodesic Computations for Fast and Accurate Surface Remeshing and Parameterization," *Progress in Nonlinear Differential Equations and Their Applications*, vol. 63, pp. 151-171, [www.ceremade.dauphine.fr/peyre](http://www.ceremade.dauphine.fr/peyre), 2005.
- [50] S. Pizer, K. Siddiqi, G. Szekely, J. Damon, and S. Zucker, "Multiscale Medial Loci and Their Properties," *Int'l J. Computer Vision*, vol. 55, nos. 2/3, pp. 155-179, 2003.
- [51] K. Polthier and M. Schmies, "Straightest Geodesics on Polyhedral Surfaces," *Proc. ACM Siggraph*, pp. 30-38, 2006.
- [52] S. Prohaska and H.C. Hege, "Fast Visualization of Plane-Like Structures in Voxel Data," *Proc. IEEE Visualization*, pp. 29-36, 2002.
- [53] C. Pudney, "Distance-Ordered Homotopic Thinning: A Skeletonization Algorithm for 3D Digital Images," *Computer Vision and Image Understanding*, vol. 72, no. 3, pp. 404-413, 1998.
- [54] D. Reniers and A. Telea, "Part-Type Segmentation of Articulated Voxel-Shapes Using the Junction Rule," *Computer Graphics Forum*, vol. 27, no. 7, pp. 1837-1844, 2008.
- [55] D. Reniers, J.J. van Wijk, and A. Telea, "Computing Multiscale Skeletons of Genus 0 Objects Using a Global Importance Measure," *IEEE Trans. Visualization and Computer Graphics*, vol. 14, no. 2, pp. 355-368, Mar. 2008.
- [56] M. Rumpf and A. Telea, "A Continuous Skeletonization Method Based on Level Sets," *Proc. Symp. Data Visualisation*, pp. 151-158, 2002.
- [57] S. Rusinkiewicz and M. Levoy, "QSPat: A Multiresolution Point Rendering System for Large Meshes," *Proc. ACM Siggraph*, pp. 230-237, 2000.
- [58] D. Shaked and A. Bruckstein, "Pruning Medial Axes," *Computer Vision and Image Understanding*, vol. 69, no. 2, pp. 156-169, 1998.
- [59] J. Shewchuk, "Triangle: Engineering a 2D Quality Mesh Generator and Delaunay Triangulator," *Proc. Workshop Applied Computational Geometry: Towards Geometric Eng.*, pp. 203-222, 1996.
- [60] K. Siddiqi, S. Bouix, A. Tannenbaum, and S. Zucker, "Hamilton-Jacobi Skeletons," *Int'l J. Computer Vision*, vol. 48, no. 3, pp. 215-231, 2002.
- [61] K. Siddiqi, S. Bouix, A. Tannenbaum, and S.W. Zucker, "The Hamilton-Jacobi Skeleton," *Proc. IEEE Int'l Conf. Computer Vision*, pp. 828-834, 1999.
- [62] K. Siddiqi and S. Pizer, *Medial Representations: Mathematics, Algorithms and Applications*. Springer, 2009.
- [63] S. Stolpner, S. Whitesides, and K. Siddiqi, "Sampled Medial Loci and Boundary Differential Geometry," *Proc. IEEE Workshop 3D Digital Imaging and Modeling*, pp. 87-95, 2009.
- [64] S. Stolpner, S. Whitesides, and K. Siddiqi, "Sampled Medial Loci for 3D Shape Representation," *Computer Vision and Image Understanding*, vol. 115, no. 5, pp. 695-706, 2011.
- [65] R. Strzodka and A. Telea, "Generalized Distance Transforms and Skeletons in Graphics Hardware," *Proc. Symp. Data Visualisation*, pp. 221-230, 2004.
- [66] A. Sud, "Efficient Computation of Discrete Voronoi Diagram and Homotopy-Preserving Simplified Medial Axis of a 3D Polyhedron," PhD thesis, Univ. of North Carolina, Chapel Hill, 2006.
- [67] A. Sud, M. Foskey, and D. Manocha, "Homotopy-Preserving Medial Axis Simplification," *Proc. ACM Symp. Solid and Physical Modeling*, pp. 103-110, 2005.
- [68] V. Surazhsky, T. Surazhsky, D. Kirsanov, S. Gortler, and H. Hoppe, "Fast Exact and Approximate Geodesics on Meshes," *Proc. ACM Siggraph*, pp. 130-138, 2005.
- [69] A. Tagliasacchi, H. Zhang, and D. Cohen-Or, "Curve Skeleton Extraction from Incomplete Point Cloud," *Proc. ACM Siggraph*, pp. 541-550, 2009.
- [70] A. Telea and A. Jalba, "Voxel-Based Assessment of Printability of 3D Shapes," *Proc. 10th Int'l Conf. Math. Morphology and Its Applications to Image and Signal Processing*, pp. 393-404, 2011.
- [71] A. Telea and J.J. van Wijk, "An Augmented Fast Marching Method for Computing Skeletons and Centerlines," *Proc. Symp. Data Visualisation*, pp. 251-259, 2002.
- [72] M. van Dortmont, H. van de Wetering, and A. Telea, "Skeletonization and Distance Transforms of 3D Volumes Using Graphics Hardware," *Proc. 13th Int'l Conf. Discrete Geometry for Computer Imagery*, pp. 617-629, 2006.
- [73] V. Verma and J. Snoeyink, "Reducing the Memory Required to Find a Geodesic Shortest Path on a Large Mesh," *Proc. 17th ACM SIGSPATIAL Int'l Conf. Advances in Geographic Information Systems*, pp. 227-235, 2009.
- [74] M. Wan, F. Dache, and A. Kaufman, "Distance-Field Based Skeletons for Virtual Navigation," *Proc. IEEE Visualization*, pp. 239-246, 2001.
- [75] J. Wang, M. Oliveira, and A. Kaufman, "Reconstructing Manifold and Non-Manifold Surfaces from Point Clouds," *Proc. ACM Symp. Solid Modeling and Applications*, pp. 139-147, 2007.
- [76] K. Zhou, Q. Hou, R. Wang, and B. Guo, "Real-Time KD-Tree Construction on Graphics Hardware," *ACM Trans. Graphics*, vol. 27, no. 5, p. 111, 2008.



computer graphics and vision, shape processing, and parallel computing.



ests include shape and surface processing with applications toward healthcare systems.



and software analytics.

**Andrei C. Jalba** received the BSc and MSc degrees in applied electronics and information engineering from the "Politehnica" University of Bucharest, Romania, in 1998 and 1999, respectively, and the PhD degree from the Institute for Mathematics and Computing Science of the University of Groningen, The Netherlands, in 2004. Currently, he is an assistant professor at the Eindhoven University of Technology, the Netherlands. His research interests include

**Jacek Kustra** received the licenciatura degree in electronics and telecommunications and the MSc degree in biomedical engineering from the University of Aveiro, Portugal, in 2004 and 2008, respectively. Currently, he is working toward the PhD degree at the University of Groningen, The Netherlands. In parallel to his studies, he worked as a software development freelancer. He is employed as a scientist at Philips Research at the University of Groningen. His research inter-

**Alexandru C. Telea** received the PhD degree in computer science from the Eindhoven University of Technology, The Netherlands in 2000. Until 2007, he was an assistant professor in visualization and computer graphics at the same university. Since 2007, he has been a professor of computer science at the University of Groningen, The Netherlands. His research interests include 3D multiscale shape processing, scientific and information visualization,

► For more information on this or any other computing topic, please visit our Digital Library at [www.computer.org/publications/dlib](http://www.computer.org/publications/dlib).